Adsorption of Helium on Small Cationic PAHs: Influence of Hydrocarbon Structure on the Microsolvation Pattern

Arne Schiller, Miriam Meyer, Paul Martini, Fabio Zappa, Serge Krasnokutski, Florent Calvo, Paul Scheier

Adsorption of Helium on Small Cationic PAHs: Influence of Hydrocarbon Structure on the Microsolvation Pattern

Arne Schiller,[*,†] Miriam Meyer,[†] Paul Martini,[†] Fabio Zappa,[†] Serge A. Krasnokutski,[‡] Florent Calvo,[¶] and Paul Scheier[†]

†*Institut für Ionenphysik und Angewandte Physik, Universität Innsbruck, Technikerstr. 25, A-6020 Innsbruck, Austria*

‡*Laboratory Astrophysics Group of the MPI for Astronomy at the University of Jena, Helmholtzweg 3, D-07743 Jena, Germany*

¶*Univ. Grenoble Alpes, CNRS, LiPhy, F-38000 Grenoble, France*

E-mail: arne.schiller@uibk.ac.at

Abstract

The adsorption of up to $\sim$ 100 helium atoms on the planar polycyclic aromatic hydrocarbons (PAHs) anthracene, phenanthrene, fluoranthene and pyrene in cationic form was studied by combining helium nanodroplet mass spectrometry with classical and quantum computational methods. Recorded time-of-flight mass spectra reveal a unique set of structural features in the ion abundance as a function of the number of attached helium atoms for each of the investigated PAHs. Path-integral molecular dynamics simulations were used with a polarizable potential to determine the underlying adsorption patterns of helium around the PAH cations and in good general agreement with the experimental data. The calculated structures of the helium-PAH complexes indicate that the arrangement of adsorbed helium atoms is highly sensitive towards the structure of the solvated PAH cation. Closures of the first solvation shell around the studied PAH cations are suggested to lie between 29 and 37 adsorbed helium atoms depending on the specific PAH cation. Helium atoms are found to preferentially adsorb on these PAHs following the $\sqrt{3} \times \sqrt{3}$ commensurate pattern common for graphitic surfaces, in contrast to larger carbonaceous molecules like corannulene, coronene and fullerenes that exhibit a 1×1 commensurate phase.

1 Introduction

The adsorption of atoms and molecules on carbonaceous materials has been widely studied for a variety of reasons, ranging from probing fundamental chemistry and physics[1–4] to practical applications like hydrogen storage.[5–7] Helium is a highly interesting adsorbant species from a fundamental standpoint due to its extremely weak binding and its quantum nature which becomes relevant at the low temperatures required to bind helium atoms.[8] Although helium is the second most abundant element in the universe by a large margin, complex formation with neutral atoms or molecules is expected to be unlikely due to its low binding energy even at the low temperatures present in most regions of the interstellar medium. The

interaction of helium with ions is much stronger and, besides physisorption, makes chemisorption also possible. In fact the helium hydride ion is considered to be the first molecule being formed in relevant quantities in the early Universe.[9] In laboratory experiments, He-tagged ions represent ideal targets for action spectroscopy, as recently demonstrated in several laboratories.[10–21] The weak binding energy leads to small line shifts with respect to the isolated ions and is at the same time a confirmation for vibrationally cold ions.

Helium adsorption has been studied extensively on graphite,[22–26] graphene[27,28] and graphene derivatives[29–32] as well as carbon nanotubes.[33,34] Going down in size, molecules such as fullerenes and polycyclic aromatic hydrocarbons (PAHs) offer the possibility to study helium adsorption on finite planar and curved graphene-like flakes. Whereas helium adsorption on neutral fullerenes has only been studied theoretically thus far,[35–43] helium adsorption on neutral PAHs has been studied using various spectroscopic and theoretical methods.[44–49]

As already mentioned, the interaction between helium atoms and ions is much stronger compared to the neutral-helium interactions due to the presence of a net charge and the resulting ion-induced polarization forces. This interaction is strongest for helium atoms closest to the ion, leading to a higher helium density in the immediate vicinity of the ion. For ions embedded in liquid helium, the helium atoms in the innermost solvation shell around an ion form a structure known as a snowball, with strongly localized helium atoms that no longer exhibit liquid, but rather solid-like character.[50] Helium-solvated ions can be studied mass spectrometrically by monitoring their yield as a function of attached helium atoms. Pronounced step-wise drops in the ion yield at specific numbers of attached He atoms indicate shell closures and intensity anomalies with respect to neighboring complexes are often designated as magic numbers, assigned to particularly stable structures. Atomistic simulations can then help to elucidate the nature of the solvation structures, provided that nuclear delocalization effects are accounted for. A combined study by Leidlmair et al. utilized mass spectrometry and quantum-corrected molecular dynamics (MD) simulations of fullerene-doped helium nanodroplets (HNDs) to study the adsorption of helium on cationic

fullerenes[51] (for a review see Refs. 52 and 8). The authors identified the formation of the highly-ordered, rigid-like 1×1 commensurate phase where each hexagonal and pentagonal face is occupied by one helium atom for $C_{60}He_{32}^+$ and $C_{70}He_{37}^+$ as well as, tentatively, the closure of the first helium solvation shell at $C_{60}He_{60}^+$ and $C_{70}He_{62}^+$. While the agreement between experiment and theory was excellent for $n = 32$, the evidence was inconclusive for the second anomaly, as the MD simulations suggested the closure of the first solvation shell of $C_{60}He_n^+$ at $n = 74$, or $n = 58$ when quantum effects are included. Independent PIMD simulations of $C_{60}He_n^+$[53] found that the addition of further helium atoms beyond $n = 32$ induce significant disorder in the 1×1 commensurate phase, forming a liquid-like layer, which becomes rigid-like once again at $n = 60$ and is finally complete at $n = 72$. Harnisch et al. performed a study of helium-decorated fullerene anions[54] and found that magic numbers observed for $C_{60}He_n^-$ and $C_{70}He_n^-$ are identical to their respective cationic counterparts, except for the second anomaly of $C_{70}He_n^-$ which is found at $n = 65$ rather than $n = 62$ as for $C_{70}He_n^+$. So far, the reason for these differences between cationic and anionic systems remains unclear.

In a subsequent study, Kuhn et al. investigated photodissociation of $C_{60}He_n^+$ upon electronic excitation for complexes containing up to $n \sim 100$ He atoms.[19] Line shifts were determined as a function of the number of He atoms attached. A remarkably linear red shift of ~ 0.07 nm per He atom was observed up to $n = 32$, followed by a nonlinear blue shift up to $n = 60$ and a less pronounced red shift up to $n = 80$. A precise understanding of the structure and binding energies of helium-ion complexes is very valuable for the interpretation of action spectra since it can be used to extrapolate the observed shift as a function of the number of He atoms down to zero, i.e. the position of the gas-phase transition.[20] A recent investigation by Gatchell et al. highlighted the interplay of mass spectrometry, action spectroscopy and path-integral molecular dynamics (PIMD) simulations to address helium solvation of corannulene cations.[55] A comprehensive theoretical study on helium coating of the three planar, cationic PAHs (pyrene, coronene and circumcoronene) as well as benzene was performed by one of us using a similar computational methodology as in the cationic

fullerene case.[56] It was found in this study that the graphitic surfaces are covered first by relatively strongly bound helium atoms which form a solid-like layer where helium atoms are highly localized above the aromatic rings. Additional helium atoms then cover the peripheral regions in the molecular plane, displaying an intermediate, 'slushy' character, before a liquid-like outer layer is formed around the molecule. Shortly after, Kurzthaler et al. published an experimental study of helium coverage of coronene cations,[57] identifying prominent step-wise intensity drops in the abundance of $C_{24}H_{12}He_n^+$ at $n = 38, 41$ and 44. These experimental results were in good agreement with a subsequent theoretical study of helium adsorption on neutral coronene performed by Rodríguez-Cantano et al., which reported enhanced stability of $C_{24}H_{12}He_n$ at $n = 38$ (for both classical and quantum calculations) and completion of the first solvation shell at $n = 44$ (only evident in quantum calculations).[49] Kurzthaler et al. thus proposed that in the $n = 38$ complex, all aromatic rings as well as the peripheral, open hexagons of coronene are covered by one helium atom each on both sides of the molecular plane, with three and six additional helium atoms added around the edge of the cation forming symmetrical structures of enhanced stability, explaining the step-wise drops at $n = 41$ and 44. These results were further confirmed by an additional PIMD study of the cationic system,[58] in which it was also shown that the additional atoms beyond $n = 38$ appeared to be strongly delocalized rather than forming well-defined, rigid-like structures. Moreover, this study suggested that $n = 44$ does not correspond to the filling of the first solvation shell, as 50 helium atoms could still be inserted in a single solvation shell, thereby possibly revealing interesting differences with the neutral case,[49] and indicating that the anomalies in the experiment may not necessarily be associated with the completion of geometric shells for these hydrocarbon cations. In the present work, we further explore the solvation of cationic PAHs by helium atoms by studying smaller PAHs than previously investigated and, for the first time, including isomeric species. All of the chosen PAHs which are anthracene (Ant) and phenanthrene (Phe), both $C_{14}H_{10}$, as well as fluoranthene (Flu) and pyrene (Pyr), both $C_{16}H_{10}$, have a planar geometry. We demonstrate the sensibility of helium solvation charac-

teristics to changes in the structure of the solvated PAH cation and further aim to emphasize the importance of interplay between experimental and theoretical work required to resolve the structure of helium-ion complexes.

2 Methods

2.1 Experimental

The experiment used for this study recently underwent reconstruction, significantly changing the ion production and ion extraction mechanisms to the point that both setups can be considered as different experiments. Detailed descriptions of the original[59] and the current setup[10] can be found elsewhere, hence we only give a brief outline here. In both experiments, a beam of HNDs with a mean size of typically a few million He atoms[60,61] is produced by expanding pre-cooled, pressurized (20–31 bar) high-purity helium (He 6.0, 99.9999% purity) through a nozzle of 5µm in diameter cooled to 8.3–9.5 K. In the original setup (used for fluoranthene and pyrene), sample molecules are evaporated from a heated oven and picked up by (or doped into) neutral HNDs. The doped, neutral droplets are subjected to electron ionization (EI), resulting in the ejection of small ions and small ionic complexes from the droplets. In the current setup (used for anthracene and phenanthrene), the HND beam is subjected to EI first, leading to the formation of highly-charged droplets with an estimated average charge state of $+10e$.[61] The highly-charged droplets subsequently pick up sample molecules that are introduced from an external heated reservoir via a heated stainless steel tube. The dopant molecules locate at the charge centers of the droplets and are ionized upon charge transfer from He_n^+. The beam of highly-charged, doped droplets then collides with a polished stainless steel surface, resulting in the ejection of ions. This method produces a much greater yield of ions complexed with up to ∼100 He atoms in comparison to the original setup.[62] In both experiments, ions are guided from the ion extraction region into a high-resolution ($m/\Delta m$ = 1500–4500) reflectron time-of-flight mass spectrometer (ToF-MS)

via weak electrostatic fields. Recorded mass spectra were analyzed using the IsotopeFit software.[63] All PAH samples were purchased from Sigma-Aldrich and have purities between 98 and 99.5%.

2.2 Computational

The same methodology already employed in an earlier investigation[56] is followed here. Briefly, the cationic PAHs are treated as rigid, with their geometries optimized using a standard quantum chemistry calculation at the level of density-functional theory using the B3LYP hybrid functional and the 6-31G(d,p) basis set.[64] The atomic charges needed to represent the electrostatic environment felt by the helium atoms were obtained by the conventional RESP procedure.[65] All optimized geometries with the corresponding set of partial charges are provided as supplementary information. The classical and quantum structures of helium clusters around these cations were simulated at the atomistic level of details, assuming the very same polarizable potential already described in Ref. 56. Basin-hopping global optimization[66] was first conducted for all clusters containing up to 50 helium atoms, using 5 series of 100 000 random collective moves and an effective temperature of 10 K for the Metropolis Monte Carlo acceptance rates. Nuclear delocalization was then included through the PIMD methodology by performing trajectories of 1 ns, of which only the last 500 ps were considered for accumulating the properties, with a time step of 0.5 fs and a Trotter delocalization number of 256, the temperature of 1 K being maintained by means of massive Nosé-Hoover thermostats. The PIMD simulations were initiated from the putative classical global minima, and periodic quenches from the centroid positions were also carried out to confirm that no new important minimum was missed. In the following, we denote by $E_{\mathrm{C}}(n)$ the binding energy of the putative global minimum associated with the structure of n helium atoms around a given cationic PAH and refer to it as the classical energy. From those simulations the quantum energies $E_{\mathrm{Q}}(n)$ were extracted from the virial estimator, and helium density plots were accumulated as well. From the classical and quantum energies, first and

second energy differences were also determined to provide a connection with experimentally measured ion abundances. Here we will particularly focus on the latter quantity evaluated as

$$\Delta_2 E(n) = E_{\mathrm{X}}(n+1) + E_{\mathrm{X}}(n-1) - 2E_{\mathrm{X}}(n) \tag{1}$$

where X = C or Q. To describe structures more conveniently, we will also refer to them using the notation $X + Y(+Z)$, where X and Y denote the number of helium atoms lying on either side of the PAH and Z, if present, the number of atoms lying in the vicinity of the PAH plane. In addition to the classical and quantum structures and their associated energies, we also explored the extent of statistical delocalization in the nuclear wavefunction probed by the PIMD simulations, by performing regular quenches from the instantaneous centroid positions. Doing so provides a number of locally stable isomers $\{i\}$ with classical energies $\{E_i\}$, each of them being found proportionally to its probability p_i. From the set of probabilities, an information entropy S_{IS} associated with these inherent structures can be evaluated as $S_{\mathrm{IS}} = -k_{\mathrm{B}} \sum_i p_i \ln(p_i)$ where k_{B} is the Boltzmann constant. $S_{\mathrm{IS}}/k_{\mathrm{B}}$ is a dimensionless number that measures the structural diversity hidden in the quantum wavefunction and is vanishing if and only if the wavefunction is associated to a single well-defined structure, which may or may not be the classical minimum.[67] Here we use this quantity as an indicator of whether the classical and quantum structures differ from one another, from a statistical perspective.

3 Results and Discussion

3.1 Mass Spectra

Figure 1 shows excerpts of two time-of-flight mass spectra of HNDs doped with fluoranthene (panel (b), recorded with the original setup) and anthracene (panel (a), recorded with the current setup), respectively. Both mass spectra extend from the respective monomer to the

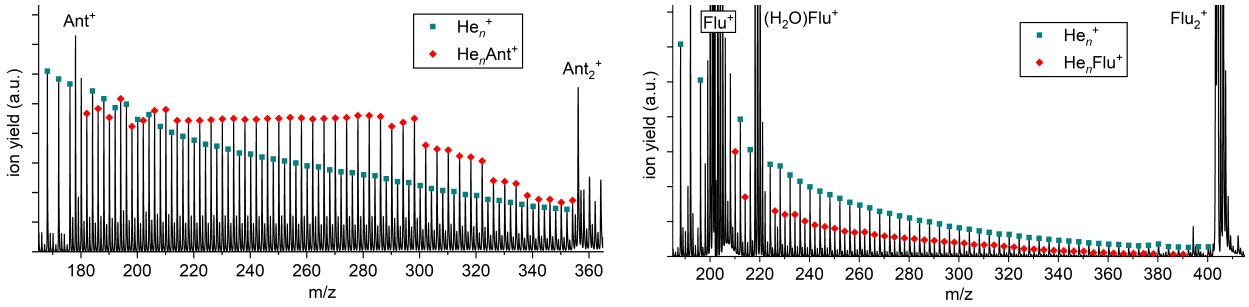

(a) (b)

Figure 1: Time-of-flight mass spectra of cationic helium-PAH complexes obtained by doping HNDs with the PAHs (a) anthracene; (b) fluoranthene. Both mass spectra reveal ion series of bare helium clusters He_n^+ (turquoise squares) and helium-decorated cations He_nPAH^+ (red diamonds), alongside contributions of bare and water-decorated PAH clusters. Differences in the overall shape of the He_nPAH^+ distribution and the relatively higher yield of He_nAnt^+ are caused by differences in the experimental setup. For details see section on experimental methods.

dimer region. The strongest signals in the fluoranthene spectrum are caused by the bare monomer and dimer as well as the monomer complexed with one water molecule picked up from the residual gas and are between one and three orders of magnitude stronger than the ion yields from He-tagged fluoranthene ions. In the region between the monomer and dimer, two weaker ion series can be found which are spaced by $\sim 4\, m/z$ and exhibit an approximately exponential decrease with increasing m/z. These two series can be attributed to bare helium clusters He_n^+ and fluoranthene monomer cations complexed with up to $\sim$50 helium atoms, He_nFlu^+. Equivalent signals can be found in the anthracene mass spectrum, but with very different relative intensities, which can be attributed to the different mechanisms of dopant ionization and extraction of ions from the helium droplets.[10] The bare monomer and dimer signals are still among the strongest ion signals, but much weaker compared to the fluoranthene mass spectrum. The $(H_2O)Ant^+$ signal is so weak that it cannot be distinguished in the presented figure. In contrast, the He_nAnt^+ series is notably stronger and no longer exhibits an apparent exponential decrease with increasing n, but rather similar ion yields between $n = 1-30$, followed by a decline in intensity above $n = 30$. Several anomalies like pronounced local maxima and step-wise drops of the ion yield can be clearly noticed

at specific numbers n. Similar features are also found in the He_nFlu^+ series but are less apparent due to the lower ion yield. Such intensity anomalies originate from changes in the respective dissociation energies of those complexes. Complexes with lower dissociation energies are more easily dissociated and thus the corresponding ion yields are depleted, whereas the ion yields of particularly stable complexes appear relatively enhanced, leading to the observed local anomalies. We distinguish between two types of local anomalies detected in the experimental: magic numbers, characterized by an anomalously high ion yield compared to both $n-1$ and $n+1$ as well as step-wise drops, characterized by a significant drop in ion yield compared to $n+1$ but not $n-1$. It should be noted that these designations can be subjective and ambiguous in some cases which is why we focus only on the more prominent features. While the He_nPAH^+ series extends to $n \sim 100$, the region $n < 40$ is most interesting for our analysis since it contains almost all of the detected features. In the following sections, we will analyze the information extracted from mass spectra in combination with computational results and thus contribute to determining the structure of the cationic PAHs anthracene, phenanthrene, fluoranthene and pyrene decorated with finite numbers of helium atoms.

3.2 Anthracene

Fig. 2a shows the ion yield of the He_nAnt^+ series (cf. Fig. 1a) as a function of n from 1 to 43 attached helium atoms. As already pointed out, the ion yield remains similar up to $n = 30$, followed by a steep decline. We immediately identify prominent magic numbers at $n = 4$ and 8 as well as step-wise drops at $n = 27$, 30, 36 and 39. In Fig. 2b, the second energy differences $\Delta_2 E(n)$ obtained in both classical and quantum descriptions are shown. Whereas the local maxima of $\Delta_2 E(n)$ at $n = 4, 8, 30$ and 36 coincide with experimentally detected anomalies, no pronounced local maxima are found for the experimentally detected anomalies at $n = 27$ and 39. The calculations further suggest the existence of anomalies at $n = 14$ and 32, which are not reflected in the mass spectra. Figure 3 depicts the corresponding classical and quantum

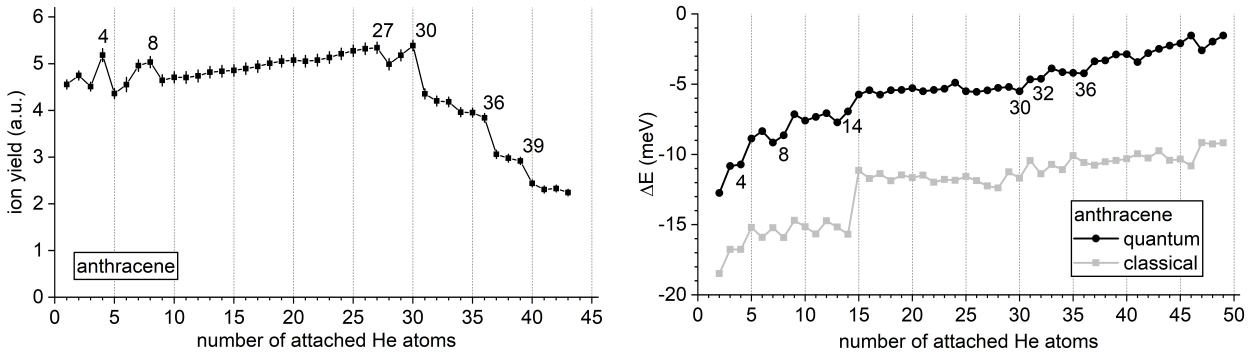

(a) (b)

Figure 2: (a) Experimental distribution of He_nAnt^+ as a function of n. Magic numbers are found at $n = 4$ and 8 with additional step-wise drops at $n = 27$, 30, 36 and 39. (b) Second energy difference $\Delta_2 E(n)$ calculated from the classical global minima (grey symbols) or from the quantum virial energies (black symbols).

structures obtained for selected sizes, from the putative global minima or the nuclear densities sampled from the PIMD trajectories, respectively. The growth pattern proceeds similarly as previously discussed for coronene,[49,56,58] and consists first of the adsorption of helium atoms on both sides of the carbon rings (2+2 pattern), then of the filling of the peripheral region closer to the PAH plane, until the shell is complete. Shell filling itself is not a sharp process but occurs in a range that depends on the number of atoms needed to fill this peripheral region and in which the binding energy varies more smoothly.

In general, the nuclear density is significantly more extended than the space covered by the classical positions, as a result of vibrational delocalization. Such an effect often produces nuclear wavefunctions that do not present the exact same symmetric features as those exhibited by the classical structure. An archetypal example is provided for the $n = 4$ complex, for which the classical minimum has two helium atoms adsorbed on both sides of the PAH, near adjacent aromatic rings, in a commensurate 1×1 fashion. Once nuclear delocalization is accounted for, the two atoms on either side expand and preferentially occupy the outer rings. Such an expansion is also manifested for the $n = 8$ complex, but now in a more lateral fashion for this cluster that adopts a 4+4 adsorption pattern, keeping the symmetry in the quantum case. At size 14, a double hexagonal filling 7+7 is predicted, also

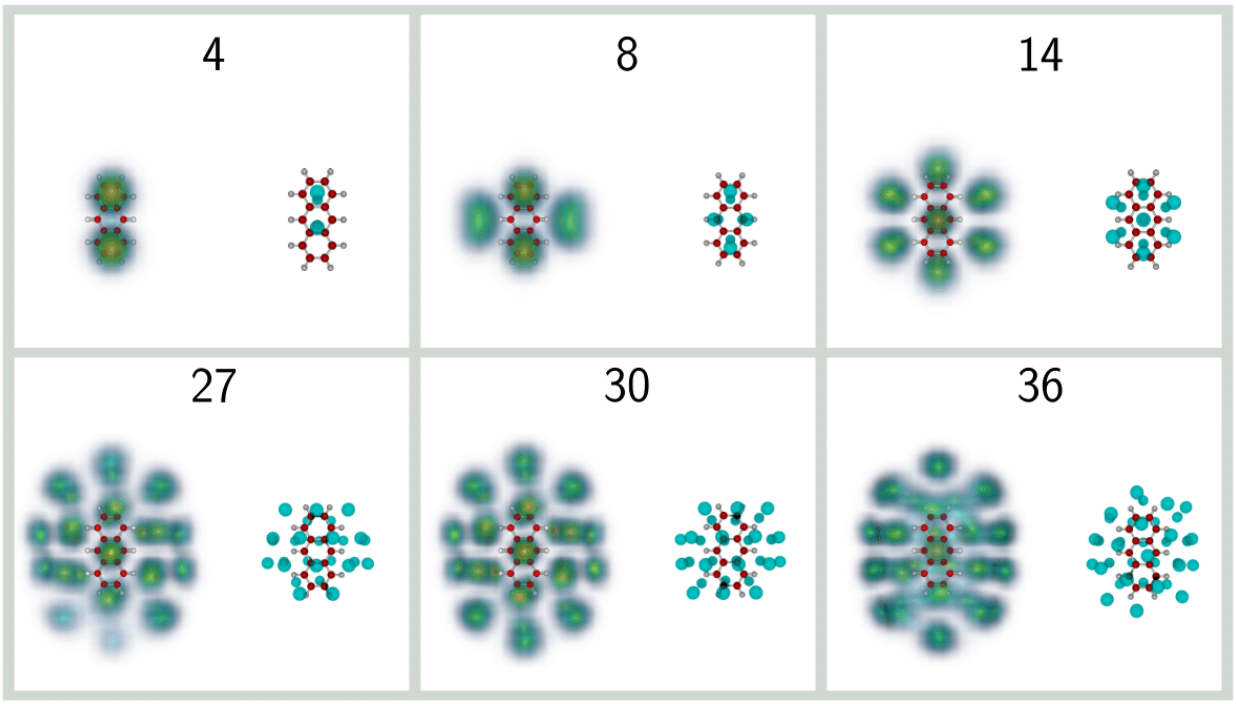

Figure 3: Selected structures of He_nAnt^+ clusters with $n = 4$, 8, 14, 27, 30, and 36. For each size, the classical global minima are shown on the right, while the helium densities obtained from the PIMD simulations are shown on the left.

closer to the $\sqrt{3} \times \sqrt{3}$ commensurate filling of helium monolayers adsorbed on graphite, in which half of the hexagonal sites are occupied. As more helium atoms are added, the solvation shell further expands, but the central hexagonal motif remains and imposes further growth. The structure obtained at size 27 is not particularly symmetric and reveals an incomplete outer shell. Our calculations indicate that shell filling begins at size 30 and ends below size 36, the cluster at this size already exhibiting some significant degree of fluxionality, with the nuclear density no longer showing well defined spots. Noteworthily, at these sizes of 30 and 36 the quantum structures display a higher symmetry degree than their classical counterparts, which also indirectly confirms their greater stability suggested by mass spectra. We thus interpret shell filling around cationic anthracene to occur in the approximate range of 30–36 attached helium atoms.

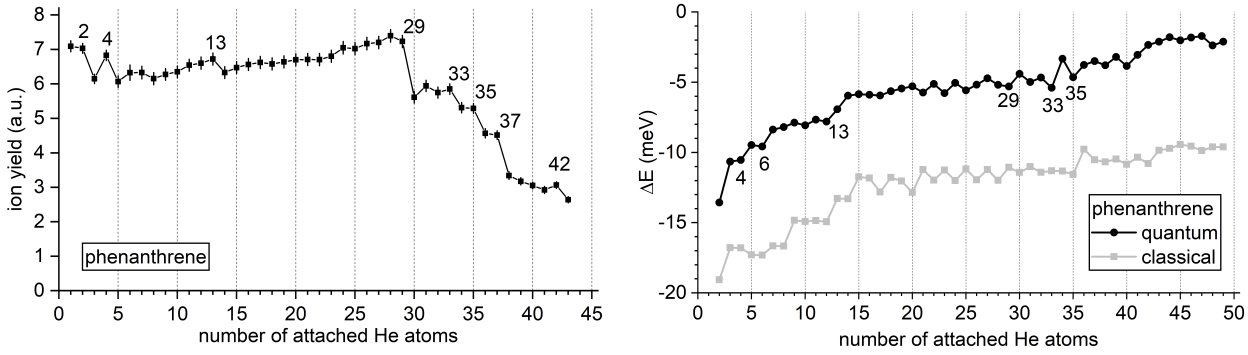

(a) (b)

Figure 4: (a) Experimental distribution of He_nPhe^+ as a function of n. Magic numbers are seen at $n = 4$ and 42, with additional step-wise drops at $n = 2$, 13, 29, 33, 35 and 37. (b) Second energy difference $\Delta_2 E(n)$ calculated from the classical global minima (grey symbols) or from the quantum virial energies (black symbols).

3.3 Phenanthrene

Fig. 4a shows the He_nPhe^+ series as a function of n from 1 to 43 attached He atoms. The overall shape is very similar to that of He_nAnt^+. Prominent magic numbers are found at $n = 4$ and a weaker one at $n = 42$ as well as step-wise drops at $n = 2$, 13, 29, 33, 35 and 37. Whereas the overall shape of the distribution is very similar to that of He_nAnt^+, the anomalies exhibit a different pattern. Both compounds share the first magic number at $n = 4$, however, there is no equivalent to the local maximum of He_nAnt^+ at $n = 8$ in the He_nPhe^+ series. Instead, a pronounced step is found at $n = 13$ which itself has no equivalent in the He_nAnt^+ series. The other features are qualitatively similar, with the most prominent step occurring at $n = 29$ for He_nPhe^+ (instead of $n = 30$ for He_nAnt^+), followed by a series of smaller steps. The smaller step-wise drops are spaced by two helium atoms for He_nPhe^+, instead of three for He_nAnt^+. A feature similar to the step at $n = 27$ in He_nAnt^+ is missing in the He_nPhe^+ series. In Figure 4b, the second energy differences $\Delta_2 E(n)$ for He_nPhe^+ are shown. The overall agreement between the progression of He_nPhe^+ and $\Delta_2 E(n)$ is good, with important features such as the anomalies at $n = 2, 4, 13, 29, 33$ and 35 being correctly captured by the quantum calculations. The prominent step at $n = 37$ is not reproduced well by theory but instead expected at $n = 38$. Also, some intermediate features are predicted

at $n = 6, 21$ and 23 but are not particularly reflected in the mass spectra.

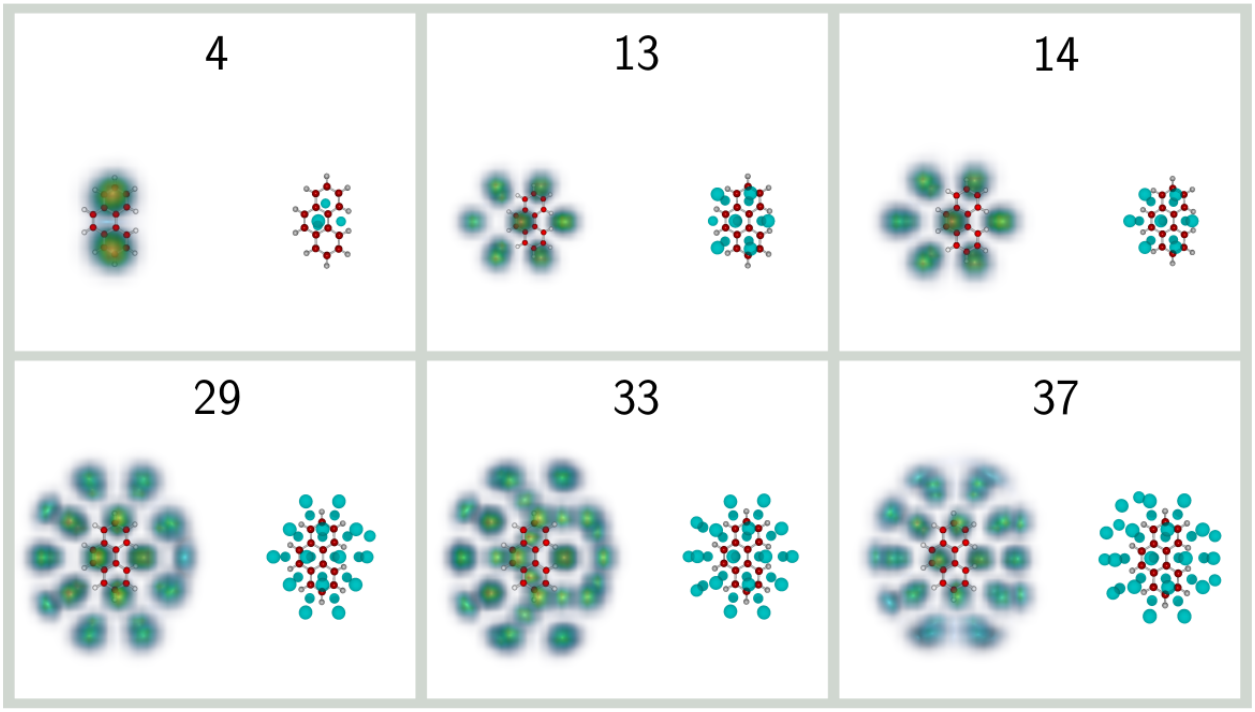

Figure 5: Selected structures of He_nPhe^+ clusters with $n = 4$, 13, 14, 29, 33 and 37. For each size, the classical global minima are shown on the right, while the helium densities obtained from the PIMD simulations are shown on the left.

The corresponding classical and quantum structures obtained for selected sizes of He_nPhe^+ are shown in Fig. 5. The different positions of the outer hexagons relative to anthracene give rise to interesting differences in physical adsorption patterns. For this PAH, the classical and quantum structures obtained for the $n = 4$ complex are at qualitative variance, being of the 3+1 and 2+2 types, respectively, as the result of competing zero-point energies. In the quantum case, the atoms are preferentially adsorbed on either side of the outer hexagons. Upon adding helium atoms, the same growth mechanisms as in the anthracene case seem to be followed, ending up at size 14 as the 7+7 hexagonal motif. However, the different topology of phenanthrene makes it energetically preferable to adsorb 13 atoms only, as 6+6 and one atom near the PAH plane (in average) and on its concave side. The extra atom leading to the more localized 7+7 system is thus found to be also more strained, and less favorable. The lower symmetry of phenanthrene is also reflected on the structure of larger

clusters, particularly at size 33 where all helium atoms still manage to occupy rather localized sites. Inherent structures also appear to be very few at size 34 [see Fig. S1 in Supporting Information], indicating very similar classical and quantum structures and a much-reduced degree of delocalization. In contrast, at size 37 the extent of vibrational delocalization has become significant and the solvation shell appears disrupted. For the phenanthrene cation, we evaluate the shell filling range as taking place between 29 and 34 He atoms.

3.4 Fluoranthene

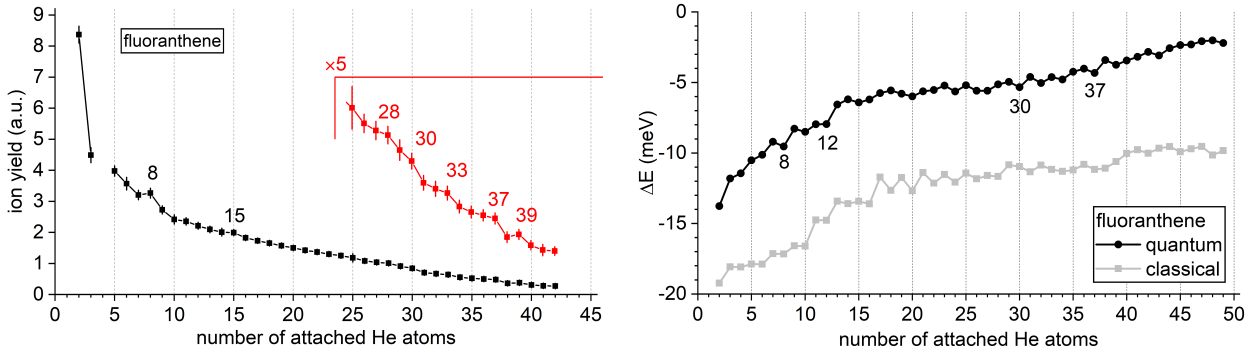

(a) (b)

Figure 6: (a) Experimental distribution of He_nFlu^+ as a function of n. Magic numbers are seen at $n = 8$, 15, 28 and 39, with additional step-wise drops at $n = 30$, 33 and 37. Missing data points are caused by the interference of isobaric ions (cf. Fig. 1b). (b) Second energy difference $\Delta_2E(n)$ calculated from the classical global minima (grey symbols) or from the quantum virial energies (black symbols).

Fig. 6a displays the distribution of He_nFlu^+ from $n = 2$ to 42. The He_nFlu^+ series exhibits a lower overall intensity and a different shape compared to both He_nAnt^+ and He_nPhe^+ series due to the different experimental setups (cf. sections on experimental methods and mass spectra). The ion yield is highest for the $n = 2$ complex and declines rapidly with increasing n, loosely resembling an exponential decay. Magic numbers are not immediately obvious but can be found upon closer inspection at $n = 8, 15, 28$ and 39, with step-wise drops occurring at $n = 30$, 33 and 37. A comparison with the calculated $\Delta_2E(n)$ shown in Fig. 6b shows reasonable agreement, with the prominent features at $n = 8, 30$ and 37

being well-captured by the calculations. However, other features do not coincide with local maxima in $\Delta_2 E(n)$, the calculations notably predicting a particularly stable structure at $n = 12$ that is not reflected in the experimental data.

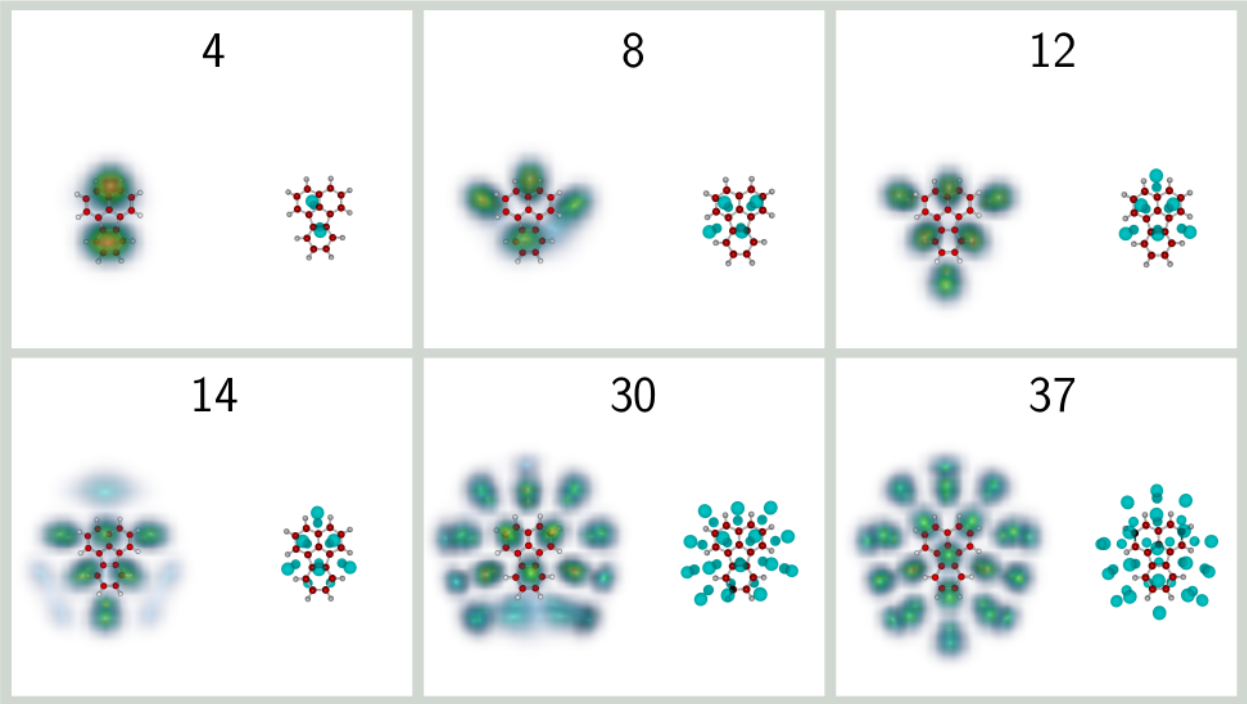

Figure 7: Selected structures of He_nFlu^+ clusters with $n = 4$, 8, 12, 14, 30, and 37. For each size, the classical global minima are shown on the right, while the helium densities obtained from the PIMD simulations are shown on the left.

The corresponding classical and quantum structures obtained for selected sizes are shown in Fig. 7 for this PAH. The peculiar topology of fluoranthene gives rise to also rather specific adsorption preferences. At both sizes 4 and 8, the helium atoms are evenly shared on both sides of the PAH, and adsorbed either on next-neighbor hexagonal rings ($n = 4$ case) or more closely packed towards the two adjacent hexagonal rings ($n = 8$ case), but always producing classical structures that are lower in symmetry than the PAH itself. Once quantum effects are accounted for, the significant expansion of the nuclear wavefunction restores this symmetry, preferred adsorption sites being now the single hexagonal ring and opposite sites lying away from the molecule (see Fig. 7). The more difficult accommodation of the adsorbed helium atoms on the fluoranthene topology is particularly obvious at size 12, which despite

still being of the 6+6 type shows a rather spectacular inversion between the classical and quantum structures. The structure obtained at $n = 14$ builds on the same pattern as the $n = 12$ complex, but differently in the classical and quantum cases, where its adsorption pattern should be better described as 6+8 or 6+6+2, respectively, two extra floating atoms exhibiting strong delocalization in the quantum structure. At size 30 a markedly different adsorption pattern is found, in which a fivefold symmetry develops, still with incomplete shell, ending at size 37 as the 16+16+5 quantum structure. Here each 16-atom arrangement can also be described as one central atom surrounded by two pentagonal rings. This fivefold symmetric structure, which is also at variance with the classical minimum, results from a non trivial combination of the natural hexagonal packing preferred by helium monolayers and the specific topology of the fluoranthene cation. It is also highly localized and is associated with a low entropy of its inherent structures [see ESI Fig. S1]. Regarding now shell completion around the fluoranthene cation, we roughly evaluate it to occur in the range of 31–37 attached helium atoms based on the results obtained around these sizes.

3.5 Pyrene

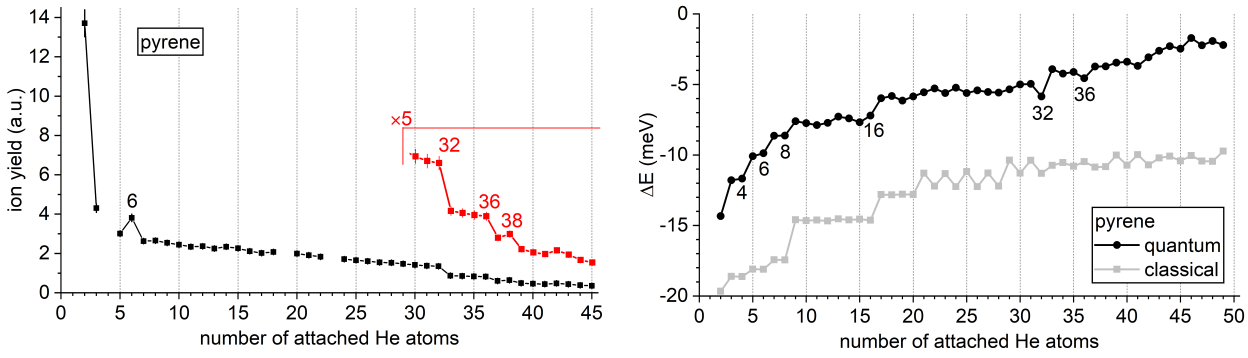

(a) (b)

Figure 8: (a) Experimental distribution of He_nPyr^+ as a function of n. Magic numbers are seen at $n = 6$ and 38, with additional step-wise drops at $n = 32$ and 36. Missing data points are caused by the interference of isobaric ions (cf. Fig. 1b). (b) Second energy difference $\Delta_2 E(n)$ calculated from the classical global minima (grey symbols) or from the quantum virial energies (black symbols).

The He_nPyr^+ series shown in Fig. 8a exhibits a similar overall shape as the He_nFlu^+ series, but with a steeper decline at $n = 2, 3$ and a slower, more linear decrease for $n \geq 7$. Local anomalies are easily identified with a pronounced magic number at $n = 6$ and a weaker one at $n = 38$ as well as two step-wise drops, a prominent one at $n = 32$ and a weaker one at $n = 36$. The strongest feature in the calculated $\Delta_2 E(n)$, shown in Figure 8b, is the strong local maximum at $n = 32$ which coincides with the most prominent step observed in the mass spectrum. The magic number at $n = 6$ is also captured by the calculations. However, the calculations do not account for the weaker step observed at $n = 36$ and the magic number at $n = 38$ but instead predict a particularly stable complex at $n = 16$ which is not reflected in the experimental data.

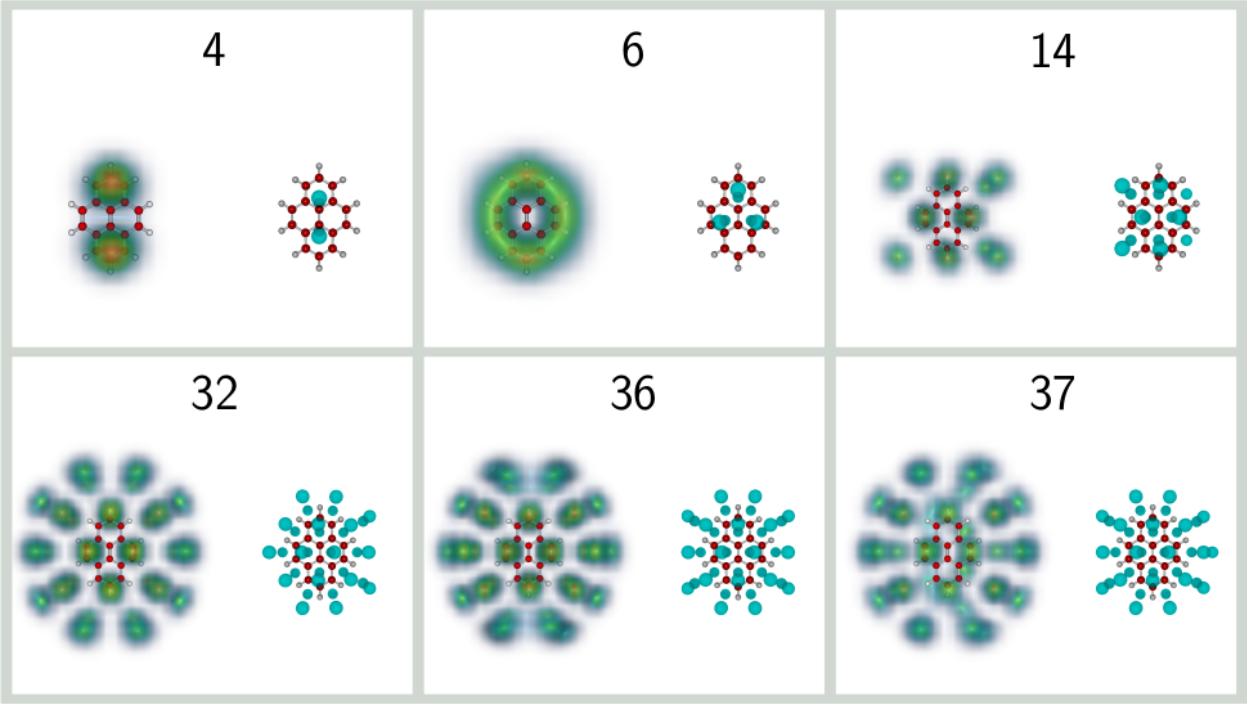

Figure 9: Selected structures of He_nPyr^+ clusters with $n = 4$, 6, 14, 32, 36, and 37. For each size, the classical global minima are shown on the right, while the helium densities obtained from the PIMD simulations are shown on the left.

The corresponding classical and quantum structures obtained for selected sizes of He_nPyr^+ are shown in Fig. 9. The $n = 4$ complex adopts a 2+2 structure in both classical and quantum case, with adsorption above the two outermost hexagonal rings. Additional helium

atoms tend to go to lateral positions, forming first a particularly stable 4+4 structure which further evolves into the 8+8 structure commensurate with the $\sqrt{3} \times \sqrt{3}$ pattern at size 16. At the intermediate size 14, this pattern is incomplete and is found as 6+8 in both classical and quantum cases. A more interesting case is that of He_6Pyr^+, which is found as a magic number in both experiment and calculations. While this system classically adopts a 3+3 structure, quantum effects produce a particularly delocalized wavefunction where the helium atoms occupy two oval rings on either side of the planar cation. Such an enhanced delocalization originates from the easy lateral motion of helium on the corrugated PAH surface, and was also noted in related systems such as He_{10}coronene$^+$ (Ref. 56) for the exact same reason. It is associated to multiple inherent structures differing in which three aromatic rings are being occupied on each side [see ESI Fig. S1]. One remarkable result for the He_6Pyr^+ complex is that nuclear delocalization is again responsible for the quantum structure exhibiting a higher symmetry than the classical counterpart, concomitant with the increased stability suggested by the experimental data. Noteworthily, none of the other $n = 6$ clusters obtained for the anthracene, phenanthrene or fluoranthene cations display such highly delocalized helium densities, despite the classical structures being also generally of the 3+3 type (2+4 for anthracene).

In larger complexes, the $\sqrt{3} \times \sqrt{3}$ core motif is preserved upon further addition of helium atoms towards the completion of the first shell. A particularly symmetric quantum structure is thus obtained at $n = 32$ as 14+14+4, and another one at $n = 36$ as 14+14+8, only the latter also showing a symmetric classical structure. Adding yet another helium atom at $n = 37$ disrupts this symmetry, and we conclude that based on our calculations, shell filling takes place in the range of 32—36 attached helium atoms for the pyrene cation.

4 Summary and Conclusion

The employed experimental and computational methods revealed a unique set of local anomalies for each of the investigated PAHs in the respective He_nPAH^+ ion series, summarized in Table 1. The best agreement between experiment and theory is found when nuclear delocalization is accounted for by using PIMD simulations, which are capable of revealing features that are not recognized by classical methods.

Table 1: Local anomalies of He_nPAH^+ complexes found via experiment and PIMD simulations employed in this study. Experimentally found anomalies are categorized as magic numbers (bold) and step-wise drops (underlined). Circled numbers represent anomalies found simultaneously in the experiment and PIMD simulations.

Local Anomalies of He_nPAH^+		
Complex	Experiment	PIMD simulations
He_nAnt^+	④, ⑧, 27, ㉚, ㊱, 39	④, ⑧, 14, ㉚, 32, ㊱
He_nPhe^+	2, ④, ⑬, ㉙, ㉝, ㉟, 37, **42**	④, 6, ⑬, ㉙, ㉝, ㉟
He_nFlu^+	⑧, **15**, **28**, ㉚, 33, ㊲, **39**	⑧, 12, ㉚, ㊲
He_nPyr^+	⑥, ㉜, ㊱, **38**	4, ⑥, 8, 16, ㉜, ㊱

While the arrangement of adsorbed helium atoms is found to be very sensitive towards the structure of the solvated PAH cation, there are also common adsorption patterns between the studied molecules. For these rather small and planar polyaromatic solutes, helium atoms preferentially adsorb following the $\sqrt{3} \times \sqrt{3}$ commensurate pattern, rather than the 1×1 fashion found for larger species such as coronene[57,58] as well as the curved corannulene,[55] or fullerenes.[51,53] In the latter two cases, the curvature of the molecules facilitates the 1×1 adsorption. For the planar coronene, however, this behavior can be attributed to a size effect, as we expect much larger PAHs to adsorb, similarly as graphitic structures, i.e. as $\sqrt{3} \times \sqrt{3}$. It would be interesting to investigate PAHs larger than coronene to see if and at what size a crossover to the $\sqrt{3} \times \sqrt{3}$ pattern can be found, or whether different factors are

responsible for the 1×1 adsorption pattern observed for coronene.

Our PIMD simulations also reveal that zero-point effects are qualitatively important in explaining many of the microsolvated structures. In particular, several quantum structures are found to exhibit a higher symmetry than the corresponding classical global minima, made possible by the expansion of the nuclear wavefunction. This occurs e.g. for $He_{32}Ant^+$, He_4Phe^+, $He_{13}Phe^+$, He_8Flu^+, $He_{37}Flu^+$, or $He_{32}Pyr^+$, and was also noted earlier in the case of $He_{38}Coronene^+$,[58] but also chemically different systems such as $(H_2)_{12}H^-$.[68]

A manifestation of the importance of quantum nuclear effects is found, for most clusters, in the diversity of inherent structures that are probed by the centroids in the PIMD trajectories, as shown by strictly positive information entropies. Even particularly stable clusters in the second energy difference are associated with multiple local minima in the energy landscape, which typically differ from each other by the specific location of the helium atoms near the peripheral region. Contrary to cationic neon clusters,[69] we found no evidence here for higher stabilities in the abundances to be associated with a locally minimum vibrational delocalization. However, the marked sensitivity to the specific PAH structure found in our measurements is well-reflected in the strong differences between the solvation patterns exhibitted by the nuclear densities, but also the inherent structure entropies obtained between the anthracene and phenanthrene cationic solutes, and those obtained between the fluoranthene and pyrene cationic solutes.

Residual discrepancies between the experimental data and our simulations could point at some approximations in our modeling that would need to be overcome in future computational developments. Besides the neglect of bosonic exchange, the rigid treatment of the hydrocarbon could be excessively simplistic, especially in the peripheral region of the PAHs where the terminating hydrogen atoms are likely prone to quantum delocalization themselves. While exchange statistics might not be essential for the present hydrocarbon solutes,[70] to which helium binds rather strongly, a flexible model would probably be more realistic in describing clusters near shell closure, as suggested by the recent work from the

Marx group on the (strongly fluxional and rather extreme) case of protonated methane.[71] To assess the importance of hydrogen delocalization and evaluate the validity of the rigid approximation used here for the cationic solutes, experiments on deuterated species could be particularly useful. We also plan to address the influence of helium solvation patterns towards spectra of electronic and vibrational transitions as observed via action spectroscopy of helium-solvated compounds in a future publication.

Acknowledgement

This work was supported by the Austrian Science Fund FWF via the projects P31149 and I4130. S.K. is grateful for the support by the Max Planck Institute for Astronomy and by the Deutsche Forschungsgemeinschaft DFG (grant No. KR 3995/4-1).

Supporting Information Available

Detailed geometries and atomic charges for the cationic PAHs are provided as supplementary material. Also included are inherent structure entropies as a function of the number of attached helium atoms as obtained from the PIMD simulations for the four cationic PAHs.

References

(1) Dabrowski, A. Adsorption — from theory to practice. *Advances in Colloid and Interface Science* **2001**, *93*, 135–224.

(2) Yang, K.; Zhu, L.; Xing, B. Adsorption of Polycyclic Aromatic Hydrocarbons by Carbon Nanomaterials. *Environmental Science & Technology* **2006**, *40*, 1855–1861.

(3) Mauracher, A.; Kaiser, A.; Probst, M.; Zöttl, S.; Daxner, M.; Postler, J.; Goulart, M. M.; Zappa, F.; Bohme, D. K.; Scheier, P. Decorating $(C_{60})_n^+$, n = 1–3,

with CO_2 at low temperatures: Sterically enhanced physisorption. *International Journal of Mass Spectrometry* **2013**, *354-355*, 271–274.

(4) Kaiser, A.; Leidlmair, C.; Bartl, P.; Zöttl, S.; Denifl, S.; Mauracher, A.; Probst, M.; Scheier, P.; Echt, O. Adsorption of hydrogen on neutral and charged fullerene: Experiment and theory. *The Journal of Chemical Physics* **2013**, *138*, 074311.

(5) Chen, P.; Wu, X.; Lin, J.; Tan, K. L. High H_2 Uptake by Alkali-Doped Carbon Nanotubes Under Ambient Pressure and Moderate Temperatures. *Science* **1999**, *285*, 91–93.

(6) Sevilla, M.; Mokaya, R. Energy storage applications of activated carbons: supercapacitors and hydrogen storage. *Energy & Environmental Science* **2014**, *7*, 1250–1280.

(7) Luo, X.-F.; Yang, C.-H.; Peng, Y.-Y.; Pu, N.-W.; Ger, M.-D.; Hsieh, C.-T.; Chang, J.-K. Graphene nanosheets, carbon nanotubes, graphite, and activated carbon as anode materials for sodium-ion batteries. *Journal of Materials Chemistry A* **2015**, *3*, 10320–10326.

(8) González-Lezana, T.; Echt, O.; Gatchell, M.; Bartolomei, M.; Campos-Martínez, J.; Scheier, P. Solvation of ions in helium. *International Reviews in Physical Chemistry* **2020**, *39*, 465–516.

(9) Lepp, S.; Stancil, P. C.; Dalgarno, A. Atomic and molecular processes in the early Universe. *Journal of Physics B: Atomic, Molecular and Optical Physics* **2002**, *35*, R57–R80.

(10) Meyer, M.; Martini, P.; Schiller, A.; Zappa, F.; Krasnokutski, S. A.; Scheier, P. Electronic Spectroscopy of Anthracene Cations and Protonated Anthracene in the Search for Carriers of Diffuse Interstellar Bands. *The Astrophysical Journal* **2021**, *913*, 136.

(11) Marks, J. H.; Miliordos, E.; Duncan, M. A. Infrared spectroscopy of RG $-$ $Co^+(H_2O)$ complexes (RG = Ar, Ne, He): The role of rare gas "tag" atoms. *The Journal of Chemical Physics* **2021**, *154*, 064306.

(12) Geistlinger, K.; Fischer, M.; Spieler, S.; Remmers, L.; Duensing, F.; Dahlmann, F.; Endres, E.; Wester, R. A sub-4 Kelvin radio frequency linear multipole wire trap. *Review of Scientific Instruments* **2021**, *92*, 023204.

(13) Verma, D.; Erukala, S.; Vilesov, A. F. Infrared Spectroscopy of Water and Zundel Cations in Helium Nanodroplets. *The Journal of Physical Chemistry A* **2020**, *124*, 6207–6213.

(14) Campbell, E. K.; Dunk, P. W. LV-DIB-s4PT: A new tool for astrochemistry. *Review of Scientific Instruments* **2019**, *90*, 103101.

(15) Davies, J. A.; Besley, N. A.; Yang, S.; Ellis, A. M. Infrared spectroscopy of a small ion solvated by helium: OH stretching region of HeN $-$ $HOCO^+$. *The Journal of Chemical Physics* **2019**, *151*, 194307.

(16) Gerlich, D.; Jašík, J.; Roithová, J. Tagging fullerene ions with helium in a cryogenic quadrupole trap. *International Journal of Mass Spectrometry* **2019**, *438*, 78–86.

(17) Günther, A.; Nieto, P.; Müller, D.; Sheldrick, A.; Gerlich, D.; Dopfer, O. BerlinTrap: A new cryogenic 22-pole ion trap spectrometer. *Journal of Molecular Spectroscopy* **2017**, *332*, 8–15.

(18) Roithová, J.; Gray, A.; Andris, E.; Jašík, J.; Gerlich, D. Helium Tagging Infrared Photodissociation Spectroscopy of Reactive Ions. *Accounts of Chemical Research* **2016**, *49*, 223–230.

(19) Kuhn, M.; Renzler, M.; Postler, J.; Ralser, S.; Spieler, S.; Simpson, M.; Linnartz, H.;

Tielens, A. G. G. M.; Cami, J.; Mauracher, A. et al. Atomically resolved phase transition of fullerene cations solvated in helium droplets. *Nature Communications* **2016**, *7*, 13550.

(20) Campbell, E. K.; Holz, M.; Gerlich, D.; Maier, J. P. Laboratory confirmation of C_{60}^+ as the carrier of two diffuse interstellar bands. *Nature* **2015**, *523*, 322–323.

(21) Asvany, O.; Brünken, S.; Kluge, L.; Schlemmer, S. COLTRAP: a 22-pole ion trapping machine for spectroscopy at 4 K. *Applied Physics B* **2014**, *114*, 203–211.

(22) Polanco, S. E.; Bretz, M. Liquefaction of 2nd-Layer He-4 Films on Graphite. *Physical Review B* **1978**, *17*, 151–158.

(23) Carneiro, K.; Passell, L.; Thomlinson, W.; Taub, H. Neutron-Diffraction Study of the Solid Layers at the Liquid-Solid Boundary in He-4 Films Adsorbed on Graphite. *Physical Review B* **1981**, *24*, 1170–1176.

(24) Greywall, D. S. Heat-Capacity and the Commensurate-Incommensurate Transition of He-4 Adsorbed on Graphite. *Physical Review B* **1993**, *47*, 309–318.

(25) Crowell, P. A.; Reppy, J. D. Reentrant Superfluidity in He-4 Films Adsorbed on Graphite. *Physical Review Letters* **1993**, *70*, 3291–3294.

(26) Crowell, P. A.; Reppy, J. D. Superfluidity and film structure in He-4 adsorbed on graphite. *Physical Review B* **1996**, *53*, 2701–2718.

(27) Pierce, M. E.; Manousakis, E. Role of substrate corrugation in helium monolayer solidification. *Physical Review B* **2000**, *62*, 5228–5237.

(28) Clements, B. E.; Krotscheck, E.; Lauter, H. J. Growth Instability in Helium Films. *Physical Review Letters* **1993**, *70*, 1287–1290.

(29) Gordillo, M. C.; Boronat, J. He-4 on a Single Graphene Sheet. *Physical Review Letters* **2009**, *102*, 085303.

(30) Markic, L. V.; Stipanovic, P.; Beslic, I.; Zillich, R. E. He-4 clusters adsorbed on graphene. *Physical Review B* **2013**, *88*, 125416.

(31) Reatto, L.; Galli, D. E.; Nava, M.; Cole, M. W. Novel behavior of monolayer quantum gases on graphene, graphane and fluorographene. *Journal of Physics-Condensed Matter* **2013**, *25*, 443001.

(32) Markic, L. V.; Stipanovic, P.; Beslic, I.; Zillich, R. E. Solidification of He-4 clusters adsorbed on graphene. *Physical Review B* **2016**, *94*, 045428.

(33) Dzyubenko, B.; Lee, H. C.; Vilches, O. E.; Cobden, D. H. Surface electron perturbations and the collective behaviour of atoms adsorbed on a cylinder. *Nature Physics* **2015**, *11*, 398–402.

(34) Wang, Z. H.; Wei, J.; Morse, P.; Dash, J. G.; Vilches, O. E.; Cobden, D. H. Phase Transitions of Adsorbed Atoms on the Surface of a Carbon Nanotube. *Science* **2010**, *327*, 552–555.

(35) Kwon, Y.; Shin, H. Superfluidity and structural order in He-4 adsorbed on a C_{20} molecule: Path-integral Monte Carlo calculations. *Physical Review B* **2010**, *82*, 172506.

(36) Hernandez, E. S.; Cole, M. W.; Boninsegni, M. Adsorption of atoms and fluids on spherical surfaces. *Physical Review B* **2003**, *68*, 125418.

(37) Barranco, M.; Hernandez, E. S.; Mayol, R.; Pi, M. Density modes in spherical He-4 shells. *Physical Review B* **2004**, *69*, 134502.

(38) Varandas, A. J. C. Helium-Fullerene Pair Interactions: An Ab Initio Study by Perturbation Theory and Coupled Cluster Methods. *International Journal of Quantum Chemistry* **2011**, *111*, 416–429.

(39) Andersson, Y.; Rydberg, H. Dispersion coefficients for van der Waals complexes, including $C_{60} - C_{60}$. *Physica Scripta* **1999**, *60*, 211–216.

(40) Varandas, A. J. C. Møller-Plesset Perturbation Energies and Distances for HeC_{20} Extrapolated to the Complete Basis Set Limit. *Journal of Computational Chemistry* **2009**, *30*, 379–388.

(41) Varandas, A. J. C. An ab initio study of the interaction between He and C_{36} with extrapolation to the one electron basis set limit. *Chemical Physics Letters* **2008**, *463*, 225–229.

(42) Park, S.; Kim, B.; Kwon, Y. Anisotropic superfluidity of He-4 on a C_{36} fullerene molecule. *Journal of Chemical Physics* **2015**, *143*, 104311.

(43) Shin, H.; Kwon, Y. Commensurate-incommensurate transition of He-4 adsorbed on a single C_{60} molecule. *Journal of Chemical Physics* **2012**, *136*, 064514.

(44) Bach, A.; Leutwyler, S.; Sabo, D.; Bacic, Z. Very large amplitude intermolecular vibrations and wave function delocalization in 2,3-dimethylnaphthalene·He van der Waals complex. *Journal of Chemical Physics* **1997**, *107*, 8781–8793.

(45) Even, U.; Jortner, J.; Noy, D.; Lavie, N.; Cossart-Magos, C. Cooling of large molecules below 1 K and He clusters formation. *Journal of Chemical Physics* **2000**, *112*, 8068–8071.

(46) Birer, O.; Moreschini, P.; Lehmann, K. K. Electronic spectroscopy of benzo[g,h,i] perylene and coronene inside helium nanodroplets. *Physical Chemistry Chemical Physics* **2008**, *10*, 1648–1657.

(47) Pentlehner, D.; Slenczka, A. Microsolvation of anthracene inside superfluid helium nanodroplets. *Molecular Physics* **2012**, *110*, 1933–1940.

(48) Whitley, H. D.; DuBois, J. L.; Whaley, K. B. Theoretical Analysis of the Anomalous Spectral Splitting of Tetracene in He-4 Droplets. *Journal of Physical Chemistry A* **2011**, *115*, 7220–7233.

(49) Rodríguez-Cantano, R.; Pérez de Tudela, R.; Bartolomei, M.; Hernández, M. I.; Campos-Martínez, J.; González-Lezana, T.; Villarreal, P.; Hernández-Rojas, J.; Bretón, J. Coronene molecules in helium clusters: Quantum and classical studies of energies and configurations. *The Journal of Chemical Physics* **2015**, *143*, 224306.

(50) Atkins, K. R. Ions in Liquid Helium. *Physical Review* **1959**, *116*, 1339–1343.

(51) Leidlmair, C.; Wang, Y.; Bartl, P.; Schöbel, H.; Denifl, S.; Probst, M.; Alcami, M.; Martin, F.; Zettergren, H.; Hansen, K. et al. Structures, Energetics, and Dynamics of Helium Adsorbed on Isolated Fullerene Ions. *Physical Review Letters* **2012**, *108*, 076101.

(52) Echt, O.; Kaiser, A.; Zottl, S.; Mauracher, A.; Denifl, S.; Scheier, P. Adsorption of Polar and Nonpolar Molecules on Isolated Cationic C_{60}, C_{70}, and Their Aggregates. *Chempluschem* **2013**, *78*, 910–920.

(53) Calvo, F. Size-induced melting and reentrant freezing in fullerene-doped helium clusters. *Physical Review B* **2012**, *85*, 060502.

(54) Harnisch, M.; Weinberger, N.; Denifl, S.; Scheier, P.; Echt, O. Adsorption of helium on isolated C_{60} and C_{70} anions. *Molecular Physics* **2015**, *113*, 2191–2196.

(55) Gatchell, M.; Martini, P.; Laimer, F.; Goulart, M.; Calvo, F.; Scheier, P. Spectroscopy of corannulene cations in helium nanodroplets. *Faraday Discussions* **2019**, *217*, 276–289.

(56) Calvo, F. Coating Polycyclic Aromatic Hydrocarbon Cations with Helium Clusters: Snowballs and Slush. *Journal of Physical Chemistry A* **2015**, *119*, 5959–5970.

(57) Kurzthaler, T.; Rasul, B.; Kuhn, M.; Lindinger, A.; Scheier, P.; Ellis, A. M. The adsorption of helium atoms on coronene cations. *Journal of Chemical Physics* **2016**, *145*, 064305.

(58) Calvo, F. Shell completion of helium atoms around the coronene cation. *Computational and Theoretical Chemistry* **2017**, *1107*, 2–6.

(59) Schöbel, H.; Bartl, P.; Leidlmair, C.; Denifl, S.; Echt, O.; Märk, T. D.; Scheier, P. High-resolution mass spectrometric study of pure helium droplets, and droplets doped with krypton. *European Physical Journal D* **2011**, *63*, 209–214.

(60) Gomez, L. F.; Loginov, E.; Sliter, R.; Vilesov, A. F. Sizes of large He droplets. *Journal of Chemical Physics* **2011**, *135*, 154201.

(61) Laimer, F.; Kranabetter, L.; Tiefenthaler, L.; Albertini, S.; Zappa, F.; Ellis, A. M.; Gatchell, M.; Scheier, P. Highly Charged Droplets of Superfluid Helium. *Physical Review Letters* **2019**, *123*, 165301.

(62) Martini, P.; Albertini, S.; Laimer, F.; Meyer, M.; Gatchell, M.; Echt, O.; Zappa, F.; Scheier, P. Splashing of larger helium nanodroplets upon surface collisions. *Physical Review Letters* **2021**, submitted.

(63) Ralser, S.; Postler, J.; Harnisch, M.; Ellis, A. M.; Scheier, P. Extracting cluster distributions from mass spectra: Isotope Fit. *International Journal of Mass Spectrometry* **2015**, *379*, 194–199.

(64) Frisch, M. J.; Trucks, G. W.; Schlegel, H. B.; Scuseria, G. E.; Robb, M. A.; Cheeseman, J. R.; Scalmani, G.; Barone, V.; Mennucci, B.; Petersson, G. A. et al. Gaussian 09 Revision E.01.

(65) Wang, J.; Cieplak, K.; Kollman, K. A. How well does a restrained electrostatic potential (RESP) model perform in calculating conformational energies of organic and biological molecules? *J. Comput. Chem.* **2000**, *21*, 1049–1074.

(66) Wales, D. J.; Doye, J. P. K. Global Optimization by Basin-Hopping and the Lowest

Energy Structures of Lennard-Jones Clusters Containing up to 110 Atoms. *J. Phys. Chem. A* **1997**, *101*, 5111–5116.

(67) Calvo, M.-C., F.; Bacchys-Montabonel Size-induced segregation in the stepwise microhydration of hydantoin and its role in proton-induced charge transfer. *J. Phys. Chem. A* **2018**, *122*, 1634–1642.

(68) Calvo, F.; Yurtsever, E. The quantum structure of anionic hydrogen clusters. *J. Chem. Phys.* **2018**, *148*, 102305.

(69) Calvo, F.; Naumkin, F. Y.; Wales, D. J. Nuclear quantum effects on the stability of cationic neon clusters. *Chem. Phys. Lett.* **2012**, *551*, 38.

(70) Kwon, Y.; Whaley, K. B. Localization of helium at an aromatic molecule in superfluid helium clusters. *J. Chem. Phys.* **2000**, *114*, 3163–3169.

(71) Brieuc, F.; Schran, C.; Uhl, F.; Forbert, H.; Marx, D. Converged quantum simulations of reactive solutes in superfluid helium: The Bochum perspective. *J. Chem. Phys.* **2020**, *152*, 210901.